

# Radio-Interferometric Image Reconstruction with Denoising Diffusion Restoration Models

M. Morales,<sup>1</sup> E. Tolley,<sup>1</sup> R. Poitevineau<sup>1</sup>

<sup>1</sup> Institute of Physics, Laboratory of Astrophysics, École Polytechnique Fédérale de Lausanne (EPFL), 1290 Sauverny, Switzerland

Accepted XXX. Received YYY; in original form ZZZ

arXiv:2601.15844v1 [astro-ph.IM] 22 Jan 2026

## ABSTRACT

Reconstructing images of the radio sky from incomplete Fourier information is a key challenge in radio astronomy. In this work, we present a method for radio interferometric image reconstruction using a data-driven prior for the radio sky based on denoising diffusion probabilistic models (DDPMs). We first train a DDPM on radio galaxy observations from the VLA FIRST survey. We create simulated VLA, EHT, and ALMA observations of radio galaxies, then use an unsupervised posterior sampling method called Denoising Diffusion Restoration Models (DDRM) to reconstruct the corresponding images, using our DDPM as a prior. Our approach is agnostic to the measured radio interferometric data and naturally incorporates the physics of the measurement process. We are able to reconstruct images with very high fidelity  $\text{PSNR} > 60$ , a marked improvement over CLEAN and similar image reconstruction methods using conditional DDPMs.

**Key words:** Machine Learning – Image Synthesis – Radio Galaxies

## 1 INTRODUCTION

The sparse layouts of radio interferometers result in an incomplete sampling of the sky in Fourier space. Aperture synthesis by radio interferometry aims to reconstruct images of the radio sky from this incomplete Fourier information. This ill-posed inverse problem requires advanced image formation algorithms and strong regularization to compensate for the missing information.

Traditional imaging in radio-interferometry has relied on the CLEAN algorithm introduced in Högbom (1974), a sparse matching pursuit algorithm. CLEAN has had many variants and improvements over the decades, such as Multi-scale CLEAN (Cornwell 2008), W-projection, W-stacking, w-snapshotting techniques (Cornwell et al. 2008; Cornwell & Perley 1992; Ord et al. 2010), which correct the non-coplanar baseline term, A-projection (Bhatnagar et al. 2008) that correct per antenna gain variation. These improvements have made CLEAN a robust algorithm that is a staple of radio-interferometric imaging. Despite CLEAN’s success it still has certain limitations. The performance relies on user-defined parameters, the imaging lacks uncertainty quantification, and complex emission can be difficult to model with CLEAN’s discrete components.

Recent machine learning approaches in radio-interferometric imaging show promising results, which often outperform CLEAN in terms of quality. Gheller & Vazza (2022) and Connor et al. (2022) developed neural networks which learn the mapping between the dirty image and the true radio sky. Schmidt et al. (2022) redefined the deconvolution problem as inpainting in Fourier space, using a residual neural network (He et al. 2016). Aghabiglou et al. (2024) developed a series of Deep Neural Networks (DNNs) and formulate reconstruction as a series of images, with each DNN taking the previous iteration’s image estimate and associated data residual as inputs.

Drozdova et al. (2024) and Wang et al. (2023) developed conditional Denoising Diffusion Probabilistic Models (DDPM; Ho et al. 2020) to deconvolve dirty images.

However, all of these machine learning methods rely on learning a specific antenna configuration. These networks must be retrained to apply to different telescopes, or even to use for observations with different observing times or pointing directions.

In this paper we present a deep learning method for interferometric image reconstruction that does not need to be trained on any specific antenna configuration, as it naturally incorporates the physics of the measurement process. We train a DDPM which learns the morphology of radio galaxies to serve as a data-driven prior, then implement image reconstruction method using a chain of conditional reconstruction steps called Denoising Diffusion Restoration (DDRM; Kawar et al. 2022) to obtain samples consistent both with the noisy observation and with the distribution of training data. We evaluate our results on using a toy reconstruction pipeline of the VLA array layout, using real observations from the VLA FIRST (Becker et al. 1995) survey.

## 2 METHODS

### 2.1 Aperture synthesis in radio interferometry

A radio interferometer measures the spatial coherence function of the electric fields measured at antenna positions  $\vec{r}_p$  and  $\vec{r}_q$  (Cornwell et al. 2008):

$$V_{pq} = \langle E(\vec{r}_p, t) E(\vec{r}_q, t)^* \rangle_t, \quad (1)$$

These measurements, usually called visibilities, are often expressed as  $V(u, v, w)$ , where  $u, v, w$  are components of the vector between the two interferometer elements expressed in units of wavelength of the radiation.

The visibilities can be related to the sky brightness distribution

\* E-mail: emma.tolley@epfl.ch

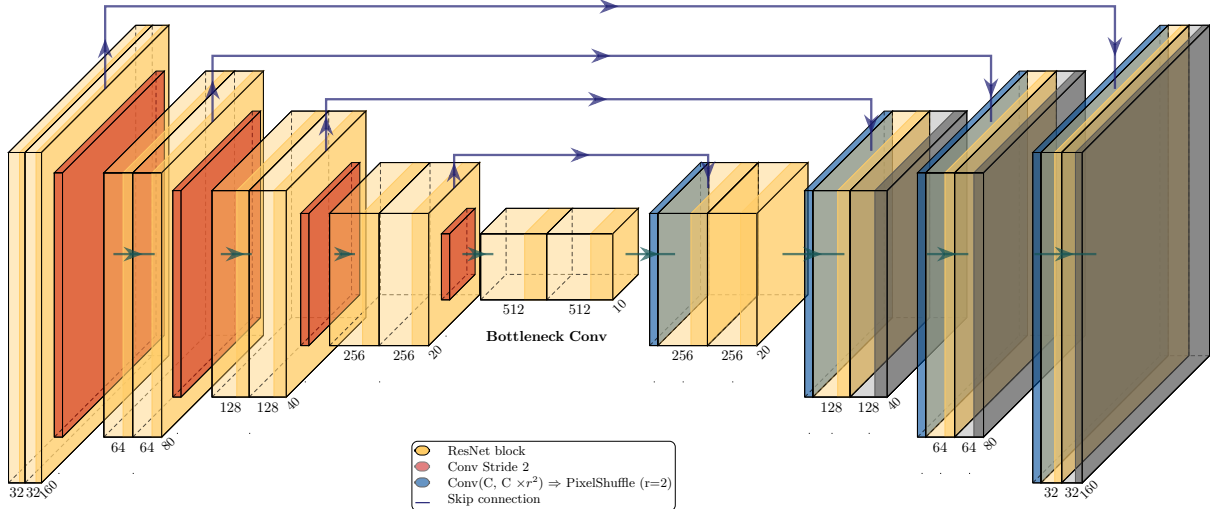


**Figure 1.** Neural Network Architecture used for the DDPM network.

$I(l, m)$  via the van Cittert-Zernike theorem (Ostrovsky et al. 2009):

$$V(u, v, w) = \iint I(l, m) e^{-2\pi i [ul + vm + wn]} \frac{dl dm}{n + 1} + z(u, v, w) \quad (2)$$

where  $n := \sqrt{1 - l^2 - m^2} - 1$  and  $\eta$  are Gaussian-distributed uncorrelated noise terms. In the small-field approximation where  $n \approx 0$ , we can rewrite this in matrix notation (Thyagarajan et al. 2017) as:

$$\mathbf{y} = \mathbf{S}\mathcal{F}\mathbf{x} + \mathbf{z}, \quad (3)$$

Where the visibilities  $\mathbf{y} \in \mathbb{C}^m$  for  $m$  antenna pairs,  $\mathbf{x} \in \mathbb{R}^n$  is the flattened radio sky image,  $\mathcal{F} \in \mathbb{C}^{n \times n}$  is the 2D Fourier transform matrix,  $\mathbf{S} \in \mathbb{C}^{m \times n}$  is the sampling matrix due to the finite number of antennas, and  $\mathbf{z} \in \mathbb{R}^m$  are uncorrelated noise terms. We note that the sampling matrix  $\mathbf{S}$  depends on the interferometer layout and observation configuration.

CLEAN starts by reconstructing an initial estimate of  $\mathbf{x}$  through back-projection, called the “dirty image”:

$$\mathbf{x}_D = \mathcal{F}^{-1}\mathbf{y} = \mathcal{F}^{-1}(\mathbf{S}) * \mathbf{x} + \mathcal{F}^{-1}\mathbf{z}, \quad (4)$$

and the “dirty beam”  $\mathcal{F}^{-1}(\mathbf{S})$  is iteratively removed from the dirty image  $\mathbf{x}_D$  by populating a model of the radio sky with discrete components, as shown in Algorithm 1.

## 2.2 Denoising Diffusion Probabilistic Models

For more details about DDPM, its theoretical foundation, capabilities, and training algorithms we refer the reader to Ho et al. (2020). The DDPM process is defined by two Markov chains, a forward (diffusion) and backwards (denoising) process. The forward process  $q(\mathbf{x}_{1:T}|\mathbf{x}_0)$  gradually adds Gaussian noise to the original data  $\mathbf{x}_0$  over  $T$  steps, producing a sequence of increasingly noisy samples  $\mathbf{x}_1, \dots, \mathbf{x}_T$ :

$$q(\mathbf{x}_{1:T}|\mathbf{x}_0) := \prod_{t=1}^T q(\mathbf{x}_t|\mathbf{x}_{t-1}) \quad (5)$$

Each transition  $q(\mathbf{x}_t|\mathbf{x}_{t-1})$  adds noise which takes the form of a Gaussian distribution with decreasing signal-to-noise ratio determined by the schedule  $\beta_t$ :

$$q(\mathbf{x}_t|\mathbf{x}_{t-1}) := \mathcal{N}(\mathbf{x}_t; \sqrt{1 - \beta_t} \mathbf{x}_{t-1}, \beta_t \mathbf{I}). \quad (6)$$

### Algorithm 1 Hogbom CLEAN

**Require:** Dirty image  $\mathbf{x}_D$ , dirty beam  $\mathbf{B}_{\text{dirty}} = \mathcal{F}^{-1}\mathbf{S}$ , stopping threshold  $\epsilon$ , loop gain  $0 < \gamma \leq 1$ , maximum iterations  $N_{\max}$

- 1: Initialize residual image:  $\mathbf{R}^{(0)} \leftarrow \mathbf{x}_D$
- 2: Initialize CLEAN component image:  $\mathbf{C} \leftarrow 0$
- 3: Set iteration counter  $k \leftarrow 0$
- 4: **while**  $\max |\mathbf{R}^{(k)}| > \epsilon \wedge k < N_{\max}$  **do**
- 5:     Find peak location:  $i_k \leftarrow \arg \max_i |\mathbf{R}^{(k)}|$
- 6:     Peak amplitude:  $a_k \leftarrow \mathbf{R}^{(k)}[i_k]$
- 7:     Add CLEAN component:  $\mathbf{C}[i_k] \leftarrow \mathbf{C}[i_k] + \gamma a_k$
- 8:     Subtract scaled dirty beam from residual:
- $\mathbf{R}^{(k+1)} \leftarrow \mathbf{R}^{(k)} - \gamma a_k \text{Shift}(\mathbf{B}_{\text{dirty}}, i_k)$
- 9:      $k \leftarrow k + 1$
- 10: **end while**
- 11:  $\mathbf{B}_{\text{clean}} \leftarrow$  2D Gaussian fit to  $\mathbf{B}_{\text{dirty}}$
- 12:  $\hat{\mathbf{x}} \leftarrow \mathbf{B}_{\text{clean}} * \mathbf{C}$
- 13: **Return** Restored image  $\hat{\mathbf{x}}$

The reverse process  $p_{\theta}(\mathbf{x}_{0:T})$  is learned by a neural network to approximate the reverse of the forward diffusion:

$$p_{\theta}(\mathbf{x}_{0:T}) := p(\mathbf{x}_T) \prod_{t=1}^T p_{\theta}(\mathbf{x}_t|\mathbf{x}_{t+1}), \quad (7)$$

where  $\theta$  refers to the parameters of the neural network. This Markov chain starts from a sample  $\mathbf{x}_T \sim \mathcal{N}(0, I)$  and attempts to remove a small amount of Gaussian noise at each step. The step function is modeled with:

$$p_{\theta}(\mathbf{x}_t|\mathbf{x}_{t+1}) := \mathcal{N}(\mathbf{x}_t; f_{\theta}(\mathbf{x}_{t+1}, t), \sigma_t^2 \mathbf{I}), \quad (8)$$

where the mean function  $f_{\theta}(\mathbf{x}_{t+1}, t)$  is the output of the neural network and  $\sigma_t^2$  is the accumulated variance noise at each timestep  $t$ . The operation is repeated  $T$  times to recover the denoised sample  $\hat{\mathbf{x}}_0$ .

### 2.2.1 Network Architecture

We implement a DDPM using a U-Net architecture Ronneberger et al. (2015), which is a multi-scale convolutional neural network with skip-connections to preserve fine detail. The network has two

parts, an encoder that progressively compresses the image to higher-level features, and a decoder that progressively reconstructs the image from these features. Each encoder and decoder block is made up of two Resnet (He et al. 2016) blocks with FiLM layers (Perez et al. 2017) after each LayerNorm (Lei Ba et al. 2016). The network has a total of 40 million free parameters. A diagram of the network architecture is shown in Figure 1.

### 2.3 Denoising Diffusion Restoration models for radio-interferometry

Kawar et al. (2022) showed that a pre-trained DDPM model can be used as a prior in a linear inversion model in order to sample from a constrained generative process:

$$p_{\theta}(\mathbf{x}_{0:T}|\mathbf{y}) := p(\mathbf{x}_T|\mathbf{y}) \prod_{t=1}^T p_{\theta}(\mathbf{x}_{t-1}|\mathbf{x}_t, \mathbf{y}), \quad (9)$$

where the measurements  $\mathbf{y}$  are obtained from the true image  $\mathbf{x}$  from a linear forward model:

$$\mathbf{y} = \mathbf{H}\mathbf{x} + \mathbf{z}, \quad (10)$$

where  $\mathbf{H}$  is the linear transformation operator and  $\mathbf{z}$  is zero-mean Gaussian noise with variance  $\sigma_y^2$ . Their solution is expressed in the singular space of the sampling operator and therefore starts with computing its singular value decomposition (SVD):

$$\mathbf{H} = \mathbf{U}\Sigma\mathbf{V}^T, \quad (11)$$

then applying the transformations  $\bar{\mathbf{y}} := \Sigma^+\mathbf{U}^T\mathbf{y}$  (where  $\Sigma^+$  is a Moore–Penrose pseudo-inverse) and  $\bar{\mathbf{x}} := \mathbf{V}^T\mathbf{x}$ . If  $f_{\theta}(\mathbf{x}_{t+1}, t)$  is the prediction made by the DDPM model at timestep  $t + 1$ , we define  $\bar{\mathbf{x}}_{\theta, t} := \mathbf{V}^T f_{\theta}(\mathbf{x}_{t+1}, t)$ . The sampling procedure then considers separately components according to the singular values of the transformation operator.

For components with zero singular value ( $s_i = 0$ ), we have no information from the measurements  $\mathbf{y}$  and sample according to the prior only:

$$p_{\theta}(\bar{\mathbf{x}}_t^{(i)} | \mathbf{x}_{t+1}, \mathbf{y}) = \mathcal{N}\left(\bar{\mathbf{x}}_{\theta, t}^{(i)} + \sqrt{1 - \eta^2} \sigma_t \frac{\bar{\mathbf{x}}_{t+1}^{(i)} - \bar{\mathbf{x}}_{\theta, t}^{(i)}}{\sigma_{t+1}}, \eta^2 \sigma_t^2\right). \quad (12)$$

When measurement is uncertain ( $\sigma_t < \sigma_y/s_i$ ), the update is guided by the measurement and weighted based on the uncertainty:

$$p_{\theta}(\bar{\mathbf{x}}_t^{(i)} | \mathbf{x}_{t+1}, \mathbf{y}) = \mathcal{N}\left(\bar{\mathbf{x}}_{\theta, t}^{(i)} + \sqrt{1 - \eta^2} \sigma_t \frac{\bar{\mathbf{y}}^{(i)} - \bar{\mathbf{x}}_{\theta, t}^{(i)}}{\sigma_y/s_i}, \eta^2 \sigma_t^2\right). \quad (13)$$

When the measurement is certain compared to the prior's variance schedule ( $\sigma_t \geq \sigma_y/s_i$ ), the variance shrinks accordingly:

$$p_{\theta}(\bar{\mathbf{x}}_t^{(i)} | \mathbf{x}_{t+1}, \mathbf{y}) = \mathcal{N}\left((1 - \eta_b)\bar{\mathbf{x}}_{\theta, t}^{(i)} + \eta_b\bar{\mathbf{y}}^{(i)}, \sigma_t^2 - \frac{\sigma_y^2}{s_i^2} \eta_b^2\right) \quad (14)$$

In all three cases  $\eta$  and  $\eta_b$  are hyperparameters that respectively control the amount of stochastic noise injected during sampling and the strength with which the measurement is enforced in the reverse process. We use  $\eta = 0.85$  and  $\eta_b = 1.0$ , following (Kawar et al. 2022).

To adapt the forward model in equation 10 and corresponding SVD for aperture synthesis, we define the transformation operator  $\mathbf{H} = \mathbf{S}\mathcal{F}$ . We first find a memory-efficient SVD of  $\mathbf{S}$  following the method presented in Kawar et al. (2022):

$$\mathbf{S} = \mathbf{I}\mathbf{K}\mathbf{P}, \quad (15)$$

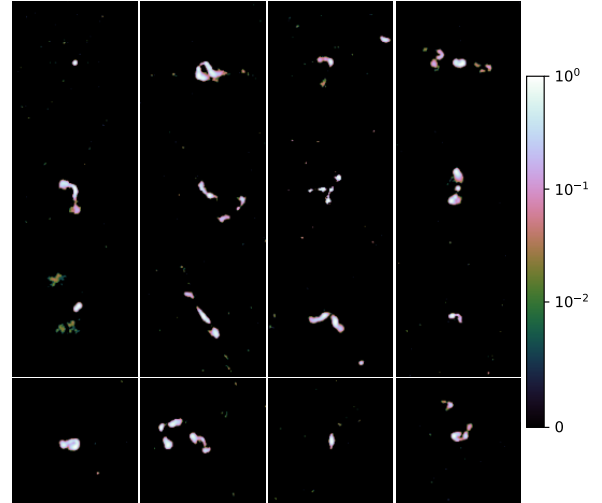


Figure 2. A selection of radio galaxies from the test dataset.

where  $\mathbf{P}$  is an appropriate permutation matrix,  $\mathbf{K}$  is a rectangular diagonal matrix of size  $m \times n$  with ones in its main diagonal, and  $\mathbf{I}$  is the identity matrix. Because  $\mathcal{F}$  is unitary, we can easily define:  $\mathbf{H} = \mathbf{U}\Sigma\mathbf{V}^T$ , where  $\mathbf{U} = \mathbf{I}$ ,  $\Sigma = \mathbf{K}$ , and  $\mathbf{V}^T = \mathbf{P}\mathcal{F}$ . This accurately represents the radio astronomy measurement equation in the small-field approximation, but does not include the effect of  $w$ –terms or  $A$ –terms.

### 2.4 Data & Training

Before using DDRM, we first need to train our DDPM model which serves as the data-driven prior. For this we used two different overlapping radio galaxy datasets. The first is a collection and combination of several catalogues using the VLA FIRST (Faint Images of the Radio Sky at Twenty-Centimeters) survey (Becker et al. 1995), curated by Griese et al. (2023). It contains galaxies identified as FRI, FRII, compact, or bent sources. We also use 20k FIRST radio galaxies from the Radio Galaxy Zoo DR1 (Wong et al. 2025). These datasets contain images of radio galaxies of size  $150 \times 150$  pixels and  $300 \times 300$  pixels, respectively. We crop the larger images to  $150 \times 150$  for consistency. The flux in both datasets is normalized to  $F_{norm} \in [-1, 1]$ . This sample of radio galaxies comprise the set of our true images  $\{\mathbf{x}\}$ . We use 200 images for validation data, 200 for test data, and 21,758 images for training following the validation and test split of Griese et al. (2023). A selection of radio galaxies from the test dataset are shown in Figure 2

For training the model, we use data augmentation, including random shifts with a maximum distance of 20 pixels, random rotation, vertical and horizontal flips, as well as multiplying each pixel in the image by a single randomly chosen value between 0.8 and 1.2, then clipped back to  $[0, 1]$  before being mapped to  $[-1, 1]$ .

We train our 40-million parameter DDPM neural network for 300'000 optimizer steps, using the DDPM training algorithm described in Ho et al. (2020). We use PyTorch's AdamW (Loshchilov & Hutter 2017) with  $\beta_1 = 0.9$  and  $\beta_2 = 0.999$  and weight decay  $1 \times 10^{-2}$ . The learning rate follows a linear schedule from optimizer step 0 to 15'000, going from  $2 \times 10^{-7}$  to  $2 \times 10^{-4}$ . Then we use a cosine annealing schedule (Loshchilov & Hutter 2016). This gives us a model that is able to generate images from our training dataset unconditionally, starting from Gaussian noise.

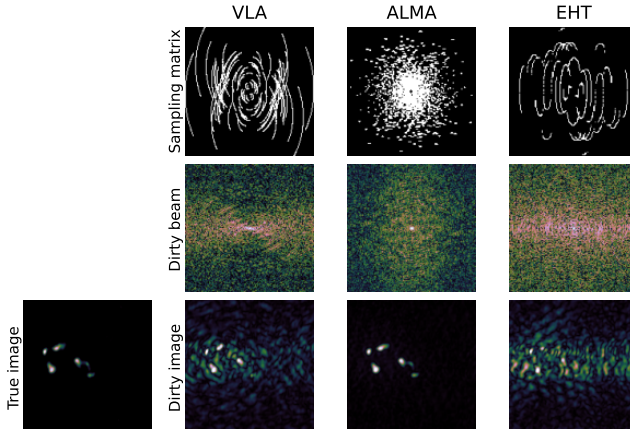


**Figure 3.** Diagram of sampling matrix  $\mathbf{S}$ , dirty beam  $\mathcal{F}^{-1}\mathbf{S}$ , true image  $\mathbf{x}$ , dirty image  $\mathbf{x}_D = \mathcal{F}^{-1}(\mathbf{S}) * \mathbf{x}$  for the three telescopes considered in this work.

## 2.5 Experimental Setup

To define a realistic sampling matrix  $\mathbf{S}$  we use three different telescope configurations:

- (i) **VLA:** We use a simulation of the Very Long Array (VLA) for 60 time steps, representing approximately 2 hours of observation time, implemented with the radio interferometer observation simulation tool from the RadioNets library (Schmidt et al. 2022).
- (ii) **EHT:** We use a sampling matrix representing the  $(u, v)$  coverage the Event Horizon Telescope (EHT; Event Horizon Telescope Collaboration 2019) telescope from Wang et al. (2023), resized to match our  $150 \times 150$  pixel input data.
- (iii) **ALMA:** We use a sampling matrix representing the  $(u, v)$  coverage the Atacama Large Millimeter Array (ALMA) from Taran et al. (2023) resized to match our  $150 \times 150$  pixel input data.

We construct the visibilities  $\{\mathbf{y}\}$  and dirty images following Eq. 4. The sampling matrix  $\mathbf{S}$ , dirty beam  $\mathcal{F}^{-1}\mathbf{S}$ , and example dirty image  $\mathbf{x}_D = \mathcal{F}^{-1}(\mathbf{S}) * \mathbf{x}$  is shown for VLA, ALMA, and EHT in Figure 3.

Once we have our measurement  $\mathbf{y} = \mathcal{F}\mathbf{x}_D$ , we then run the DDRM sampling algorithm using our trained DDPM model following the methodology described in Section 2.3 to reconstruct a clean image of the radio sky.

### 2.5.1 Comparison to Hogbom Clean

We also compare the DDRM restoration results to Hogbom CLEAN. We use a custom implementation of the classical CLEAN algorithm which includes convolution with the restoring beam. We implement CLEAN as shown in Algorithm 1. We run the algorithm with gain of  $\gamma = 0.2$  and a threshold  $\epsilon = 5 \times 10^{-7}$ , and a maximum number of 1000 iterations. We find that increasing the number of iterations and lowering the threshold does not significantly affect the results.

## 2.6 Metrics

We use three metrics for evaluating the quality of the results. The first is Mean Squared Error (MSE), defined as:

$$\text{MSE} = \frac{1}{NM} \sum_{i=1}^N \sum_{j=1}^M \left( \mathbf{x}^{(j)} - \hat{\mathbf{x}}_i^{(j)} \right)^2, \quad (16)$$

where  $\mathbf{x}$  is our true image,  $\hat{\mathbf{x}}_i$  is our  $i$ th prediction, and  $j$  indexes the  $M$  pixels of the image. We also report the peak signal-to-noise ratio

(PSNR) for comparison to other methods, defined as:

$$\text{PSNR} = 10 \times \log_{10} \left( \frac{\text{MAX}}{\text{MSE}} \right), \quad (17)$$

where  $\text{MAX} = 1$  for all images in our dataset, and the signal-to-noise ratio (SNR) defined as:

$$\text{SNR} = 10 \times \log_{10} \left( \frac{\frac{1}{N} \sum_j \mathbf{x}^{(j)}}{\text{MSE}} \right) \quad (18)$$

Finally, we evaluate the standardised reconstruction error (SRE), by measuring the reconstruction error relative to the reconstruction variability:

$$\text{SRE} = \frac{1}{NM} \sum_{i=1}^N \sum_{j=1}^M \frac{|\hat{\mathbf{x}}_i^{(j)} - \mathbf{x}^{(j)}|}{\sigma^{(j)}} \quad (19)$$

where  $\sigma^{(j)}$  is the per-pixel standard deviation map:

$$\sigma^{(j)} = \sqrt{\mathbb{E} \left[ (\hat{\mathbf{x}}^{(j)} - \mathbb{E}[\hat{\mathbf{x}}^{(j)}])^2 \right]}. \quad (20)$$

Like MSE, the SRE penalizes large errors in solution, but also takes into account if the predicted solution is within the empirical reconstruction variability.

## 3 RESULTS

After training our DDPM on the training data, we evaluate the DDRM reconstruction on the test data. The results of our image reconstruction with DDRM and CLEAN are shown in Figure 4. With DDRM we obtain images that convincingly look like the images pre-degradation. Compared to CLEAN, DDRM is able to reconstruct the central morphology of the sources with impressive accuracy and no remaining dirty beam artifacts. Overall the MSE of the DDRM reconstruction is two orders of magnitude smaller than the residuals of the CLEAN reconstruction, as shown in Figure 5.

DDRM will occasionally miss low-flux components of the images in the reconstruction. However, these low-flux components often appear in the standard deviation map of the DDRM reconstructions, indicating that DDRM is occasionally able to recover these components.

### 3.1 Sampling steps & reconstruction quality

We evaluate the image reconstruction results for different numbers of sampling steps of the DDRM algorithm. Here, the number of sampling steps refers to the number of discrete iterations used during the reverse procedure. Sampling with  $K$  timesteps where  $K < T$  means selecting  $K$  timesteps of our complete diffusion schedule  $\beta$ . Sampling with a larger number of steps should yield better results at the cost of more time, while using fewer timesteps would trade quality for sampling time. We also evaluate the time to process the sampling steps, calculated using one NVIDIA GH200 GPU on the CSCS Alps infrastructure.

The results are shown in Table 1. We find that MSE improves with higher values of  $K$ , whereas SRE does not depend as strongly on the number of sampling steps. The best MSE of  $5.2 \times 10^{-7}$  is achieved with the maximum sampling steps  $T = 1000$ . However, an excellent MSE of  $3.2 \times 10^{-5}$  is achieved with only 10 sampling steps, which can run in 0.44s, demonstrating the efficiency of DDRM.

However, we find that when reducing the number of sample steps, it is less likely that DDRM recovers faint image components.

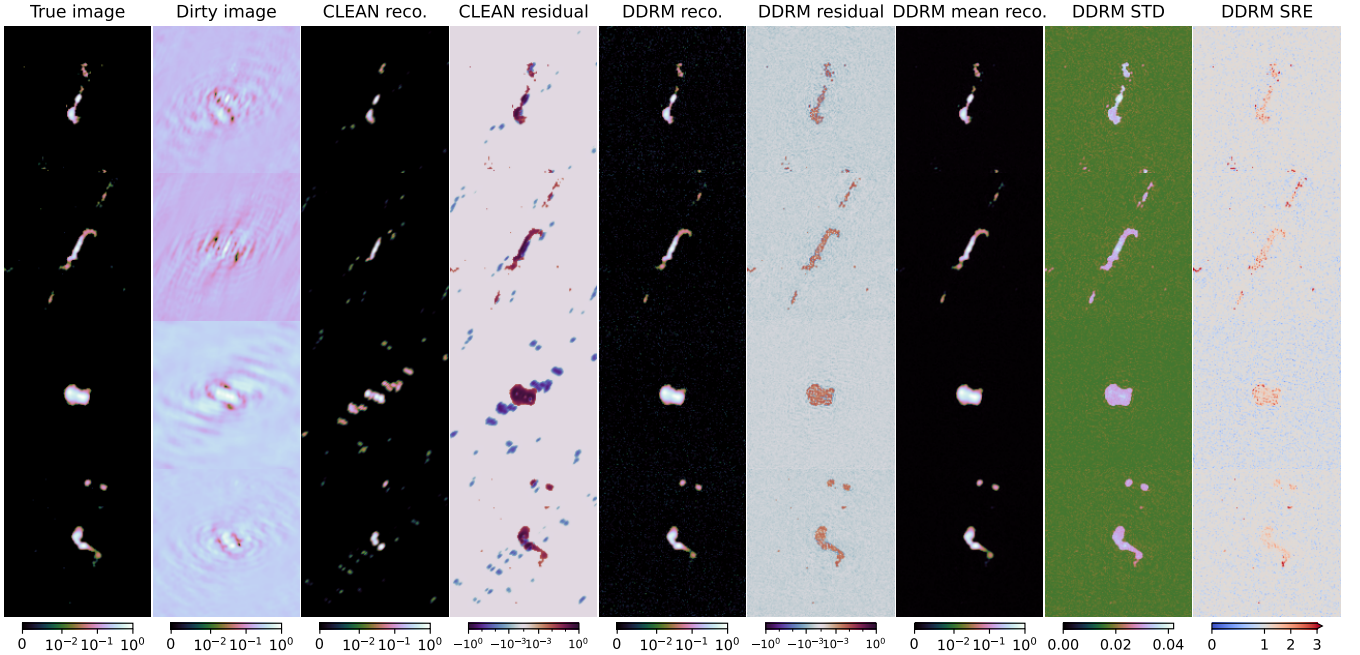


**Figure 4.** Reconstruction results for 4 example radio galaxies from the test data set using a simulated VLA observation. Columns from left to right are: the true image  $\mathbf{x}$ , the dirty image  $\mathbf{x}_D$ , the CLEAN restored image, the residual between the clean image and the true image, the DDRM reconstructed image, the residual between the DDRM image and the true image, the mean DDRM image, the per-pixel standard deviation map, and the SRE. The plots in the last three columns are calculated across 128 DDRM reconstructions.

$K$	MSE	PSNR	SNR	SRE	$t_{\text{sampling}}$ (s)
<b>VLA array configuration</b>					
10	$3.2 \times 10^{-5}$	45.0	36.8	1.39	0.44
50	$1.0 \times 10^{-5}$	49.9	41.7	1.548	2.21
100	$6.6 \times 10^{-6}$	51.8	43.7	1.40	4.41
500	$1.0 \times 10^{-6}$	59.8	51.7	1.44	22.03
1000	$5.2 \times 10^{-7}$	62.9	54.7	1.04	45.47
<b>EHT array configuration</b>					
1000	$6.8 \times 10^{-7}$	61.7	53.5	1.11	-
<b>ALMA array configuration</b>					
1000	$5.25 \times 10^{-7}$	62.8	54.6	1.14	-

**Table 1.** MSE, PSNR, SNR, SRE, and the sampling time  $t_{\text{sampling}}$  as a function of number of sampling steps  $K$ . For every  $K$  the batch size is 128. We note that 99% of the pixels in the ground truth image have very small flux values, below 5% of the maximum value.

### 3.2 Uncertainty estimation

DDPMs are often used to quantify and model uncertainty in various applications because of their inherent ability to learn the entire data distribution and therefore generate diverse, realistic samples that capture a range of possible outcomes. We evaluate how well the DDPM prior can accurately represent the reconstruction error through the SRE, which measures the reconstruction error relative to the variation in the reconstructions. A well-calibrated network should have  $\text{SRE} \leq 1$ .

We show the standard deviation of 128 reconstructions and the SRE in the two leftmost columns of Figure 4. We find that overall the DDRM is overconfident, with values of up to  $\text{SRE} = 8$  where the DDRM image reconstruction has failed to recover low-flux com-

ponents of the target image. This result is not surprising, as DDPMs are by default uncalibrated (Pang et al. 2023), ie variations in model outputs are smaller than the residuals. Section 4 presents a discussion of possible improvements and calibration methods.

### 3.3 Comparison to other machine learning methods

The conditional DDPM developed by Wang et al. (2023) was tested in image reconstruction with a simulated observation of the Event Horizon Telescope, and were able to achieve a PSNR of 20. We test our model on the same sparse  $uv$  coverage and are able to achieve a PSNR of 55.7, a significant improvement in reconstruction quality.

The conditional DDPM developed by Drozdova et al. (2024) uses an ALMA 12-m array simulation, which has much more complete  $uv$  coverage compared to the VLA or the EHT. They report a best PSNR of  $\sim 42.5$ , whereas our DDRM method is able to reconstruct images with a PSNR of 62.9. We note that Drozdova et al. (2024) included noise in their mock observation pipeline which we do not, but their reconstruction metrics did not change significantly when they varied the noise.

The RNN series developed by Aghabiglou et al. (2024) use the VLA configuration and report an SNR of  $\sim 34$ . With our DDRM reconstruction method we find an average SNR of 47.06.

## 4 DISCUSSION & CONCLUSIONS

In this work, we present a new approach to radio interferometric image reconstruction using DDRMs. Our approach is agnostic to the measured radio interferometric data and naturally incorporates the physics of the measurement process and the noise model. The DDRM algorithm can propose a range of plausible restorations for

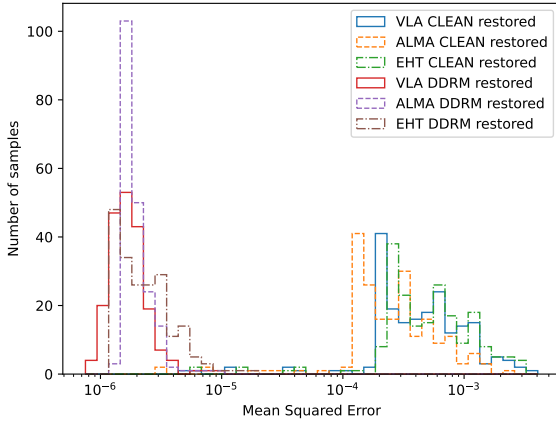


**Figure 5.** Histogram of the Mean Squared Error (MSE) distributions for CLEAN and DDRM reconstructions. DDRM consistently reconstructs images with better MSE compared to CLEAN.

the sub-sampled images typically recovered in radiointerferometry. The method is less dependent than the CLEAN algorithm on user input, and we also find that images are reconstructed with better MSE compared to CLEAN. We further find that this reconstruction method produces images with better PSNR compared to similar conditional DDPMs.

We note that we do not perform any hyperparameter optimization, and the performance could be improved by searching over different network architectures, learning rate schedules, or the  $\eta$  hyperparameters of DDRM.

While we use a DDPM prior trained exclusively on VLA images, we note that the DDRM method can easily be used with a different DDPM such as the one developed by Vičánek Martínez et al. (2024) trained on the LOFAR Two-Metre Sky Survey (LoTSS; Shimwell et al. 2022) or the one developed by Potevineau et al. (2026) trained on MeerKAT data.

Despite the impressive accuracy of the DDRM reconstruction, there are several limitations:

**Image size:** An inherent constraint of the DDRM reconstruction method is the image size, limited to  $150 \times 150$  pixel images, unlike CLEAN which can be run of images of any size. We are limited to this image size by the available training data of our DDPM. Simulated radio continuum survey maps such as (Vičánek Martínez et al. 2025) could provide larger image sizes to serve as a basis for training.

**Uncertainty:** We did not find that the range of DDRM predictions accurately represented the reconstruction error, and therefore cannot be used as an image uncertainty. This could be improved by calibrating the DDPM (Pang et al. 2023). Recent work by (Teneggi et al. 2023) has shown that conformal prediction can give finite-sample, distribution-free uncertainties for diffusion models. This method allows calibration of uncertainty thresholds on held-out data.

**Transformation operator:** DDRM relies on finding the SVD of the linear transformation operator  $\mathbf{H}$ . In this work we considered a relatively simple transformation consisting of a 2D Fourier transform and  $(u, v)$  sampling. However, contemporary imaging techniques used in radio interferometry need to account for  $A$ -terms  $W$ -terms (Bhatnagar et al. 2008; Cornwell et al. 2008), related to the direction-dependent antenna response and sky curvature, respectively. The DDRM method could be extended to include  $W$ -terms by instead using the non-uniform discrete Fourier transform (NUDFT; Bagchi &

Mitra 1999). Similarly,  $A$ -terms could be accounted for by including a matrix operator representing multiplication of the sky brightness by the primary beam  $\mathbf{A}$ :

$$\mathbf{y} = \mathbf{S}\mathcal{F}_{\text{NUDFT}}\mathbf{A} \mathbf{x}, \quad (21)$$

extending Equation 3, though a new memory-efficient SVD would need to be defined for this operator.

## ACKNOWLEDGMENTS

ET acknowledges financial support from the SNSF under the Starting Grant project Deep Waves (218396). RP acknowledges financial support from the SNSF under the Weave/Lead Agency project Radio-Clusters (214815). This work was supported by the Swiss National Supercomputing Centre (CSCS) under project ID sk031, done in partnership with the SKACH consortium through funding by SERI.

## DATA AVAILABILITY

Details on the datasets which we used for training are available in Gries et al. (2023) and (Wong et al. 2025). The code for training and inference of the model is available at <https://github.com/epfl-radio-astro/diffusionRI.git>

## REFERENCES

Aghabiglou, A., Chu, C. S., Dabbech, A., & Wiaux, Y., 2024. The R2D2 Deep Neural Network Series Paradigm for Fast Precision Imaging in Radio Astronomy, *The Astrophysical Journal Supplement Series*, **273**(1), 3.

Bagchi, S. & Mitra, S. K., 1999. *The Nonuniform Discrete Fourier Transform and Its Applications in Signal Processing*, The Springer International Series in Engineering and Computer Science, Springer, New York, NY, 1st edn.

Becker, R. H., White, R. L., & Helfand, D. J., 1995. The first survey: faint images of the radio sky at twenty centimeters, *Astrophysical Journal* v. 450, p. 559, **450**, 559.

Bhatnagar, S., Cornwell, T. J., Golap, K., & Uson, J. M., 2008. Correcting direction-dependent gains in the deconvolution of radio interferometric images, *Astronomy & Astrophysics*, **487**(1), 419–429.

Connor, L., Bouman, K. L., Ravi, V., & Hallinan, G., 2022. Deep radio-interferometric imaging with POLISH: DSA-2000 and weak lensing, *MNRAS*, **514**(2), 2614–2626.

Cornwell, T. J., 2008. Multiscale clean deconvolution of radio synthesis images, *IEEE Journal of Selected Topics in Signal Processing*, **2**(5), 793–801.

Cornwell, T. J. & Perley, R. A., 1992. Radio-interferometric imaging of very large fields. The problem of non-coplanar arrays., *A&A*, **261**, 353–364.

Cornwell, T. J., Golap, K., & Bhatnagar, S., 2008. The noncoplanar baselines effect in radio interferometry: The w-projection algorithm, *IEEE Journal of Selected Topics in Signal Processing*, **2**(5), 647–657.

Drozdova, M., Kinakh, V., Bait, O., Taran, O., Lastufka, E., Dessauges-Zavadsky, M., Holotyak, T., Schaefer, D., & Voloshynovskiy, S., 2024. Radio-astronomical image reconstruction with a conditional denoising diffusion model, *A&A*, **683**, A105.

Event Horizon Telescope Collaboration, 2019. First M87 Event Horizon Telescope Results. II. Array and Instrumentation, *ApJ*, **875**(1), L2.

Gheller, C. & Vazza, F., 2022. Convolutional deep denoising autoencoders for radio astronomical images, *MNRAS*, **509**(1), 990–1009.

Gries, F., Kummer, J., Connor, P., Brüggen, M., & Rustige, L., 2023. First radio galaxy data set containing curated labels of classes fri, frii, compact and bent, *Data in Brief*, **47**, 108974.

He, K., Zhang, X., Ren, S., & Sun, J., 2016. Deep Residual Learning for Image Recognition, in *2016 IEEE Conference on Computer Vision and Pattern Recognition (CVPR)*, p. 1.

He, K., Zhang, X., Ren, S., & Sun, J., 2016. Deep residual learning for image recognition, in *2016 IEEE Conference on Computer Vision and Pattern Recognition (CVPR)*, pp. 770–778.

Ho, J., Jain, A., & Abbeel, P., 2020. Denoising diffusion probabilistic models. *Högbom, J. A., 1974. Aperture Synthesis with a Non-Regular Distribution of Interferometer Baselines, A&AS, 15, 417.*

Kawar, B., Elad, M., Ermon, S., & Song, J., 2022. Denoising diffusion restoration models, in *Advances in Neural Information Processing Systems*.

Lei Ba, J., Kiros, J. R., & Hinton, G. E., 2016. Layer Normalization, *arXiv e-prints*, p. arXiv:1607.06450.

Loshchilov, I. & Hutter, F., 2016. SGDR: Stochastic Gradient Descent with Warm Restarts, *arXiv e-prints*, p. arXiv:1608.03983.

Loshchilov, I. & Hutter, F., 2017. Decoupled Weight Decay Regularization, *arXiv e-prints*, p. arXiv:1711.05101.

Ord, S. M., Mitchell, D. A., Wayth, R. B., Greenhill, L. J., Bernardi, G., Gleadow, S., Edgar, R. G., Clark, M. A., Allen, G., Arcus, W., Benkevitch, L., Bowman, J. D., Briggs, F. H., Bunton, J. D., Burns, S., Cappallo, R. J., Coles, W. A., Corey, B. E., deSouza, L., Doeleman, S. S., Derome, M., Deshpande, A., Emrich, D., Goeke, R., Gopalakrishna, M. R., Herne, D., Hewitt, J. N., Kamini, P. A., Kaplan, D. L., Kasper, J. C., Kincaid, B. B., Kocz, J., Kowald, E., Kratzberg, E., Kumar, D., Lonsdale, C. J., Lynch, M. J., McWhirter, S. R., Madhavi, S., Matejek, M., Morales, M. F., Morgan, E., Oberoi, D., Pathikulangara, J., Prabu, T., Rogers, A. E. E., Roshi, A., Salah, J. E., Schinkel, A., Udaya Shankar, N., Srivani, K. S., Stevens, J., Tingay, S. J., Vaccarella, A., Waterson, M., Webster, R. L., Whitney, A. R., Williams, A., & Williams, C., 2010. Interferometric imaging with the 32 element murchison wide-field array, *Publications of the Astronomical Society of the Pacific*, **122**(897), 1353–1366.

Ostrovsky, A. S., Martínez-Niconoff, G., Martínez-Vara, P., & Olvera-Santamaría, M. A., 2009. The van Cittert-Zernike theorem for electromagnetic fields, *Optics Express*, **17**(3), 1746.

Pang, T., Lu, C., Du, C., Lin, M., YAN, S., & Deng, Z., 2023. On calibrating diffusion probabilistic models, in *Thirty-seventh Conference on Neural Information Processing Systems*.

Perez, E., Strub, F., de Vries, H., Dumoulin, V., & Courville, A., 2017. FiLM: Visual Reasoning with a General Conditioning Layer, *arXiv e-prints*, p. arXiv:1709.07871.

Potvin, R., Tolley, E., & Etsebeth, V., 2026. A Guided Unconditional Diffusion Model to Synthesize and Inpaint Radio Galaxies from FIRST, MGCLS and Radio Zoo, *arXiv e-prints*, p. arXiv:2601.07485.

Ronneberger, O., Fischer, P., & Brox, T., 2015. U-Net: Convolutional Networks for Biomedical Image Segmentation, *arXiv e-prints*, p. arXiv:1505.04597.

Schmidt, K., Geyer, F., Fröse, S., Blomenkamp, P.-S., Brüggen, M., de Gasperin, F., Elsässer, D., & Rhode, W., 2022. Deep learning-based imaging in radio interferometry, *A&A*, **664**, A134.

Shimwell, T. W., Hardcastle, M. J., Tasse, C., Best, P. N., Röttgering, H. J. A., Williams, W. L., Botteon, A., Drabent, A., Mechev, A., Shulevski, A., van Weeren, R. J., Bester, L., Brüggen, M., Brunetti, G., Callingham, J. R., Chyží, K. T., Conway, J. E., Dijkema, T. J., Duncan, K., de Gasperin, F., Hale, C. L., Haverkorn, M., Hugo, B., Jackson, N., Mevius, M., Miley, G. K., Morabito, L. K., Morganti, R., Offringa, A., Oonk, J. B. R., Rafferty, D., Sabater, J., Smith, D. J. B., Schwarz, D. J., Smirnov, O., O'Sullivan, S. P., Vedantham, H., White, G. J., Albert, J. G., Alegre, L., Asabere, B., Bacon, D. J., Bonafede, A., Bonnassieux, E., Brienza, M., Billicki, M., Bonato, M., Calistro Rivera, G., Cassano, R., Cochrane, R., Croston, J. H., Cuciti, V., Dallacasa, D., Danezi, A., Dettmar, R. J., Di Gennaro, G., Edler, H. W., Enßlin, T. A., Emig, K. L., Franzen, T. M. O., García-Vergara, C., Grange, Y. G., Gürkan, G., Hajduk, M., Heald, G., Heesen, V., Hoang, D. N., Hoeft, M., Horellou, C., Iacobelli, M., Jamrozy, M., Jelić, V., Kondapally, R., Kukreti, P., Kunert-Bajraszewska, M., Magliocchetti, M., Mahatma, V., Małek, K., Mandal, S., Massaro, F., Meyer-Zhao, Z., Mingo, B., Mostert, R. I. J., Nair, D. G., Nakoneczny, S. J., Nikiel-Wroczyński, B., Orrú, E., Pajdosz-Śmierciak, U., Pasini, T., Prandoni, I., van Piggelen, H. E., Rajpurohit, K., Retana-Montenegro, E., Riseley, C. J., Rowlinson, A., Saxena, A., Schrijvers, C., Sweijen, F., Siewert, T. M., Timmerman, R., Vaccari, M., Vink, J., West, J. L., Wołowska, A., Zhang, X., & Zheng, J., 2022. The LOFAR Two-metre Sky Survey. V. Second data release, *A&A*, **659**, A1.

Taran, O., Bait, O., Dessauges-Zavadsky, M., Holotyak, T., Schaefer, D., & Voloshynovskiy, S., 2023. Challenging interferometric imaging: Machine learning-based source localization from uv-plane observations, *A&A*, **674**, A161.

Teneggi, J., Tivnan, M., Webster Stayman, J., & Sulam, J., 2023. How to Trust Your Diffusion Model: A Convex Optimization Approach to Conformal Risk Control, *arXiv e-prints*, p. arXiv:2302.03791.

Thyagarajan, N., Beardsley, A. P., Bowman, J. D., & Morales, M. F., 2017. A generic and efficient e-field parallel imaging correlator for next-generation radio telescopes, *Monthly Notices of the Royal Astronomical Society*, **467**(1), 715–730.

Vičánek Martínez, T., Baron Perez, N., & Brüggen, M., 2024. Simulating images of radio galaxies with diffusion models, *Astronomy and Astrophysics*, **691**, A360.

Vičánek Martínez, T., Edler, H. W., & Brüggen, M., 2025. Simulating realistic radio continuum survey maps with diffusion models, *A&A*, **700**, A18.

Wang, R., Chen, Z., Luo, Q., & Wang, F., 2023. A conditional denoising diffusion probabilistic model for radio interferometric image reconstruction, in *Proceedings of the 26th European Conference on Artificial Intelligence (ECAI 2023)*, vol. 372 of *Frontiers in Artificial Intelligence and Applications*, pp. 2499–2506, IOS Press.

Wong, O. I., Garon, A. F., Alger, M. J., Rudnick, L., Shabala, S. S., Willett, K. W., Banfield, J. K., Andernach, H., Norris, R. P., Swan, J., Hardcastle, M. J., Lintott, C. J., White, S. V., Seymour, N., Kapińska, A. D., Tang, H., Simmons, B. D., & Schawinski, K., 2025. Radio Galaxy Zoo data release 1: 100185 radio source classifications from the FIRST and ATLAS surveys, *MNRAS*, **536**(4), 3488–3506.

This paper has been typeset from a *TeX/LaTeX* file prepared by the author.